Exchange bias without directional anisotropy in permalloy/CoO bilayers

Alexander Mitrofanov,[1] Guanxiong Chen,[1] Alexander Kozhanov,[2] and Sergei Urazhdin[1,*]
[1]*Department of Physics, Emory University, Atlanta, Georgia 30322, USA*
[2]*Duke Quantum Center, Department of Electrical and Computer Engineering, Duke University, Durham, North Carolina 27708, USA*

(Received 18 June 2021; revised 19 August 2021; accepted 4 October 2021; published 14 October 2021)

We utilize transverse ac susceptibility measurements to characterize magnetic anisotropy in archetypal exchange-bias bilayers of ferromagnet permalloy (Py) and antiferromagnet CoO. Unidirectional anisotropy is observed for thin Py but becomes negligible at larger Py thicknesses, even though the directional asymmetry of the magnetic hysteresis loop remains significant. Additional magnetoresistance measurements, magneto-optical imaging, as well as micromagnetic simulations show that these surprising behaviors are likely associated with asymmetry of spin-flop distribution created in CoO during Py magnetization reversal, which facilitates the rotation of the latter back into its field-cooled direction. Our findings suggest possibilities for efficient realization of multistable nanomagnetic systems for neuromorphic applications

DOI: 10.1103/PhysRevB.104.144413

I. INTRODUCTION

Intense research in nanomagnetism has facilitated dramatic improvements in information storage and data processing technologies, owing to increasing memory densities and read and write speeds. In hard disks and magnetic random access memory, information is stored in the magnetization state of bistable nanomagnets [1], where magnetocrystalline, interfacial, and/or shape anisotropies produce a magnetic energy barrier between stable magnetization states. To ensure long-term stability, the barrier must significantly exceed thermal energy $k_B T = 25$ meV for devices operating at room temperature (RT) $T = 295$ K. Here, k_B is the Boltzmann constant.

Advances in materials science have enabled effective anisotropy fields exceeding 1 T, resulting in anisotropy barriers approaching 100 μeV per magnetic atom [2,3]. This energy scale sets the ultimate limit for the minimal magnetically stable volume to $\sim 10^4$ atoms. In practice, the anisotropy barrier is lowered by imperfections and inhomogeneous magnetization states formed during magnetization reversal [4].

Even for the largest achievable magnetic anisotropies, the associated energy density is three orders of magnitude smaller than the exchange energy, $\sim$100 meV per atom for transition-metal ferromagnets (FMs) [5]. If exchange could be utilized to stabilize the magnetization state, 10 magnetic atoms would be sufficient to store a bit of information. Such a small volume is impractical for the magnetoresistive electronic readout of individual magnetic bits. Nevertheless, exchange-dominated large-scale magnetic energy landscape may stabilize a multitude of magnetic configurations in a nanoscale volume, facilitating efficient implementation of nonbinary neuromorphic nanodevices such as magnetic memristors [6–9].

Ultrasmall multistable nanomagnetic systems based on exchange interaction can be developed by taking advantage of magnetic frustration. Indeed, the ground state of geometrically frustrated spin systems is massively degenerate [10]. However, geometrically frustrated spin systems rely on a subtle balance of structural and electronic effects, which may be too delicate for robust RT device applications. In randomly frustrated magnetic systems such as spin glasses, random exchange interactions produce a hierarchical energy landscape, resulting in a multitude of Gibbs states [11]. Unfortunately, conventional dilute spin glasses are not amenable to efficient magnetoelectronic control and detection of magnetic state required for the memristor operation.

Thin-film FM/antiferromagnet (FM/AFM) heterostructures may provide an alternative to spin glasses that can combine frustration effects with efficient control and detection of the magnetization state [12]. Indeed, FM layers in such heterostructures are amenable to magnetoelectronic readout and can be manipulated by spin torque [13], while the frustration of exchange interaction at the FM/AFM interface, generally expected due to the incompatibility between FM and AFM magnetic orderings [14,15], can result in glassy behaviors stabilizing a multitude of magnetization states [13,16,17]. In the simple limit of nanostructures where the FM is in the single-domain state, these configurations are characterized by multiple stable orientations of its magnetization **M**, instead of just two states stabilized by the uniaxial anisotropy. The effects of frustrated exchange interaction in such systems can be tailored by the magnetic properties and thicknesses of individual layers and by the strength of their coupling [18].

FM/AFM bilayers have been extensively studied in the context of *exchange bias* (EB)—asymmetry of the hysteresis loop observed upon field-cooling [19–21]. The EB effect is generally understood as a consequence of the formation of stable uncompensated AFM magnetic moments at the FM/AFM interface. Their exchange interaction with the magnetization **M** of the FM can be described as an effective exchange field H_E shifting the hysteresis loop of the latter. The "pinning" of **M** due to EB has found extensive applications in magnetic recording and sensing [22].

*surazhd@emory.edu

Neuromorphic applications of FM/AFM heterostructures require the ability to stabilize multiple magnetization configurations and efficiently switch among them. However, a generally accepted picture of the microscopic spin state in FM/AFM systems, necessary for its efficient manipulation, has not yet emerged. Instead, numerous competing models have been developed over more than 60 years of relevant research, as discussed in multiple reviews [20–25]. Below, we outline only the models that we believe are most directly relevant to our findings.

Mauri *et al.* [26] proposed that the reversal of the magnetization **M** of the FM in FM/AFM bilayers results in "winding" of an exchange spring in the AFM, i.e., twisting of the Néel order through the AFM thickness due to the exchange coupling at its interface with the FM. The difference in energy between the "wound" and the "unwound" states can be interpreted as the effective Zeeman energy associated with the EB field H_E. This model was supported by the experimental observations of partial rotation of AFM spins due to the reversal of **M** [27,28].

In a qualitatively different approach, Malozemoff [14] suggested that the frustrated exchange interaction at the FM/AFM interfaces can be described as a random effective field acting on the AFM, resulting in the formation Imry-Ma domains [29]. Conversely, the frustrated exchange interaction should be also manifested as an effective random field acting on the FM, which has been experimentally confirmed [15,30,31]. For small AFM thicknesses, Malozemoff [32] predicted a crossover to the Heisenberg domain state (HDS), in which the AFM domain sizes become smaller than the domain wall (DW) widths, so the Néel order becomes twisted everywhere. Such a crossover was recently experimentally observed [18], and HDS was identified as a *correlated spin glass state*—a state that exhibits short-range AFM spin correlations but lacks long-range ordering—formed below a certain material-dependent thickness of the AFM [17,33].

In yet another insight, Koon [34] showed that the exchange energy at the FM/AFM interface is minimized by the AFM *spin flop*—rotation of the Néel order into the direction orthogonal to **M**, accompanied by tilting of the AFM magnetic sublattices in the direction of **M** or opposite to it, depending on the sign of the FM/AFM exchange. Schulthess and Butler [35] pointed out that, according to this picture, reversal of **M** should result in the reversal of the AFM spin tilting, leading to the uniaxial rather than the unidirectional anisotropy. Indeed, large uniaxial anisotropy is commonly observed in FM/AFM bilayers [20,24].

It is currently believed that some varied combinations of the proposed EB mechanisms are likely responsible for a variety of experimental observations for different FM/AFM systems. However, to the best of our knowledge, the microscopic mechanisms most relevant to specific materials or systems have not yet been identified.

Here, we present experimental results that allow us to tentatively identify the mechanisms governing the magnetization states in a "classic" extensively studied EB system comprising the AFM CoO and a model low-anisotropy FM alloy $Ni_{80}Fe_{20}$ = permalloy (Py). Our main result is highly counterintuitive: Unidirectional anisotropy is observed for thin Py but vanishes for thicker Py, even though the asymmetry of the hysteresis loop persists. We use several additional complementary characterization techniques and micromagnetic simulations to show that our results are in fact simultaneously consistent with all the theoretical models outlined above, with one caveat—the exchange springlike behaviors of Mauri *et al.* [26] are likely associated with magnetic history-dependent distribution of local AFM moments rather than a coherent twist of the Néel order. Our findings provide a microscopic insight into frustrated magnetism that may become crucial for the efficient implementation of neuromorphic nanodevices based on FM/AFM heterostructures.

This paper is organized as follows. In the next section, we provide details on the sample fabrication and our experimental approach. In Sec. III, we present our experimental results. In Sec. IV, we introduce a microscopic model of the studied system and present the results of micromagnetic simulations based on this model, which capture the salient features of our experimental observations. Section V summarizes our findings.

II. MATERIALS AND EXPERIMENTAL METHODS

A. Sample preparation

CoO(8)Py(t)Ta(2) multilayers, with the Py thickness t varied between 20 and 50 nm, were grown on silicon substrates at RT, in a high-vacuum sputtering system with the base pressure of 5×10^{-9} Torr. Numbers in parenthesis are thicknesses in nanometers. Ta(2) served as a capping layer protecting the films from oxidation. The thickness of 8 nm for CoO was above the transition to the HDS at ≈6 nm, minimizing the glassy magnetic dynamics of the AFM magnetic order driven by the Py magnetization reversal [18,33]. Nevertheless, our data provide evidence for the spin-flop reversal in the AFM, which is not directly related to the glassy dynamics of the HDS [35].

The multilayers were deposited in a 150 Oe in-plane magnetic field, which is known to facilitate magnetic ordering in simple oxide AFMs CoO and NiO [36]. Since the Néel temperature $T_N = 290$ K of CoO is below the deposition temperature, this cannot be explained by "setting" of EB as, for example, is common for AFM = IrMn deposited on top of the FM in a saturating field. We speculate that in-field deposition of CoO and NiO results in a small uniaxial strain due to the magnetostriction, which facilitates the alignment of the magnetic anisotropy defined by the small lattice distortion below T_N [24].

The Py and Ta layers were deposited by dc sputtering from the stoichiometric targets in 1.8 mTorr of ultrapure Ar, while CoO was deposited from a Co target by reactive sputtering in a mixture of ultrapure oxygen and Ar, with optimized partial pressure of oxygen, as described in our previous studies of CoO-based systems [15,18,33,37]. Measurements below $T_N = 290$ K of CoO were performed after cooling from RT in the presence of an external magnetic field $H_{dc} = 0.5$ kOe.

B. Transverse ac susceptibility

The transverse ac susceptibility technique is utilized to precisely characterize the magnetic anisotropy, by detecting the oscillations of magnetization in response to the ac field $\mathbf{h}_{ac}(t) = \sqrt{2}\mathbf{H}_{ac}\cos\omega t$, with the saturating dc field $\mathbf{H}_{dc}$

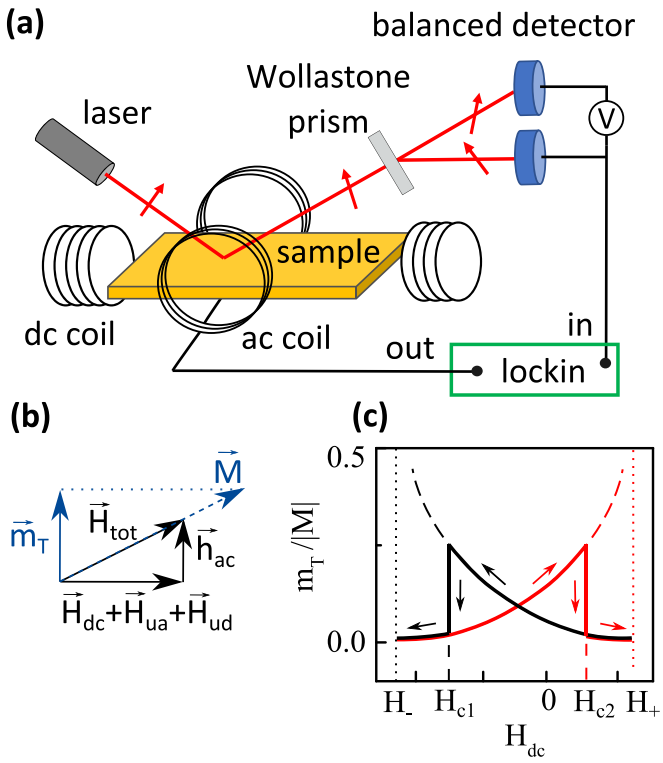

FIG. 1. (a) Schematic of the magneto-optical Kerr effect (MOKE) setup combining transverse ac susceptibility and longitudinal dc magnetometry. (b) Effective magnetic fields that determine the instantaneous orientation of the magnetization **M** in the quasistatic limit, when the frequency of the ac field $\mathbf{h}_{ac}$ is far below ferromagnetic resonance (FMR). (c) Calculated ac susceptibility vs dc field, in the presence of uniaxial and unidirectional anisotropies. The dotted vertical lines show the fields at which the extrapolated linear susceptibility diverges. The dashed vertical lines show the coercive fields.

applied perpendicular to it [33,38–41]. All the results presented below were obtained using $H_{ac} = 8$ Oe rms at the frequency $\omega/2\pi = 1.3$ kHz. Our ac susceptibility measurement setup schematically shown in Fig. 1(a) utilizes the magneto-optical Kerr effect (MOKE) to detect the oscillating component of magnetization driven by $\mathbf{h}_{ac}$. The component $M_{\parallel}$ of **M** along the dc field is also measured, allowing us to simultaneously obtain the usual longitudinal magnetic hysteresis loop. The sample is placed on the cold finger fabricated from undoped Si to minimize the inductive shunting of the ac field. All the fields are in plane, with $\mathbf{H}_{dc}$ produced by an external electromagnet, and $\mathbf{h}_{ac}$ generated by a coil built into the cold finger to minimize artifacts due to induction.

A *p*-polarized laser beam with the spot size of ∼2 mm is incident on the sample at an angle of 45° to the film surface, with $\mathbf{H}_{dc}$ in the incidence plane, and $\mathbf{h}_{ac}(t)$ perpendicular to it. The polarization of the beam reflected by the magnetic film is rotated due to the longitudinal MOKE effect, with the rotation angle proportional to $M_{\parallel}$ [42]. The Kerr polarization rotation is detected using a balanced photodetector scheme, with a Wollastone prism used to split the beam into two orthogonally polarized beams. The intensity of the beam reflected by the sample also oscillates due to transversal MOKE associated with the oscillating in-plane magnetization component $m_{\perp}(t)$ perpendicular to the incidence plane [42,43]. This intensity oscillation is detected by the lock-in amplifier connected to the output of one of the photodetectors. Thus, our setup allows a simultaneous measurement of the longitudinal Kerr effect (polarization rotation) associated with the component of magnetization collinear with the dc field and transversal Kerr effect (reflected intensity modulation) associated with the component of magnetization modulated by the ac field.

The measurement geometry of transverse susceptibility is the same as in the FM resonance (FMR) technique, which utilizes a microwave field perpendicular to the dc field to resonantly drive the magnetization oscillations. In the ac susceptibility measurements, the frequency of the ac field is typically in the hertz or kilohertz range, far below the FMR. In this quasistatic limit, the resonant dynamical properties of the FM are irrelevant. Its magnetization **M** simply follows the net effective magnetic field comprising the external field and the effective anisotropy field, allowing one to precisely characterize the latter as follows.

Consider an FM/AFM bilayer cooled in field $H_{cool} > 0$ that sets the directions of the effective unidirectional field H_{ud} and the effective uniaxial anisotropy field H_{ua} accompanying EB. We define these fields by the corresponding contributions to the total magnetic energy of the FM per unit volume averaged through its thickness, $E_M = -M[(H_{dc} + H_{ud})\cos\theta + H_{ua}\cos^2\theta/2]$, where θ is the angle between the magnetization and the effective fields.

The magnetization **M** of the FM oscillates in phase with the ac field $h_{ac}(t)$, following the direction of the total field $\mathbf{H}_{eff} + \mathbf{h}_{ac}(t)$, as shown in Fig. 1(b). We have verified that the out-of-phase component of the oscillating magnetization for the studied samples was negligible compared with the in-phase component. In the limit $h_{ac} \ll H_{eff}$ applicable to our measurements, the oscillating magnetization component is $m_T(t) \approx |M|h_{ac}(t)/H_{eff} = \sqrt{2}M_T\cos\omega t$, where M_T is the rms amplitude of this component. Normalizing by the total magnetization,

$$\frac{M_T}{|M|} = \frac{H_{ac}}{|H_{eff}|} = \frac{H_{ac}}{|H_{dc}| + H_{ua} \pm H_{ud}}. \quad (1)$$

The + (−) sign in the denominator corresponds to a saturated state at $H_{dc} > 0$ (<0). The transverse ac magnetic susceptibility χ_T was defined in some prior studies as the ratio of the amplitude of the ac magnetization component to the amplitude of the ac field [33,38,40,41]. However, in contrast to the linear susceptibility of demagnetized systems measured in the absence of dc fields, this quantity by itself is not fundamentally significant since its value depends on the magnetization and the dc field. In contrast, the response characterized by M_T/M is dimensionless and directly reflects the geometric aspects of the measurement. Below, we colloquially refer to both this quantity and M_T as the transverse susceptibility.

The dependence of M_T/M on H_{dc} described by Eq. (1) is schematically shown in Fig. 1(c). Starting at a large $H_{dc} > 0$ along the direction of the cooling field, M_T increases with decreasing H_{dc} and may be expected to diverge at $H_{dc} \equiv H_- = -H_{ua} - H_{ud}$, which corresponds to the loss of stability. In practice, the magnetization reverses at the coercive field $H_{C1} > H_-$.

In the reversed magnetization state, the effective uniaxial anisotropy field changes sign, while the effective unidirectional anisotropy field remains the same. Thus, as the dc field is increased from a large negative value, M_T/M increases and is extrapolated to diverge at $H_+ = H_{ua} - H_{ud}$, but the magnetization reverses at $H_{C2} < H_+$. Based on the above relations, the effective unidirectional and uniaxial anisotropy fields can be obtained from H_- and H_+ determined by fitting the measured $M_T(H_{dc})/M$ with Eq. (1), as $H_{ud} = (H_+ + H_-)/2$, $H_{ua} = (H_+ - H_-)/2$.

If the effective anisotropy fields are noncollinear with $\mathbf{H}_{dc}$, then $\mathbf{H}_{eff}$ forms a finite angle ψ with $\mathbf{H}_{dc}$. To the linear order in H_{ac}/H_{eff}, the ac susceptibility is then reduced by a factor of $\cos(\psi)$. This effect is minimized at large H_{dc}.

Some of the prior studies of transverse ac susceptibility analyzed the dependence $\chi_T^{-1}(H_{dc})$, or equivalently $M_T^{-1}(H_{dc})M$, the inverse of the quantity discussed here [38,40,41]. According to Eq. (1), these dependences are linear and extrapolate to the intercepts H_+ and H_-, simplifying the analysis. However, this approach places larger weight on small ac signals at large H_{dc}, leading to a larger error in the determination of H_+ and H_-.

In the studies of EB based on hysteresis loop measurements, a different set of characteristics termed *EB field* and *coercivity* are commonly introduced, defined as $H_{EB} = (H_{C2} + H_{C1})/2$ and $H_C = (H_{C2} - H_{C1})/2$, respectively. The main result of this paper is that the relation between these two sets of parameters describing EB is dependent on the thickness of the FM, revealing the microscopic mechanisms of EB in the studied system.

C. Magneto-optical imaging

Magneto-optical microscopy [43,44] was utilized to verify that the effects observed in transverse susceptibility measurements cannot be attributed to some complex inhomogeneous magnetization states and to elucidate the reversal mechanism. In our custom-built MOKE microscopy setup, light produced by a 430 nm light-emitting diode passes through a collimating system, which includes a rectangular diaphragm whose image is focused in the backplane of the 50× objective with 0.85 numeric aperture and is shifted from its axis to define the average incidence angle ∼40°. A polarizing beamsplitter is used to polarize the incident light in the incidence plane and to direct the reflected light to the detection path, which includes an analyzer, a lens, and a camera. Real-time imaging with the temporal resolution of ∼15 ms is limited by the sensitivity of the camera, and the spatial resolution of ∼250 nm is diffraction limited. A two-stage Peltier cooling system enables variable-temperature measurements, with the base temperature of 218 K.

D. Magnetoresistive characterization

Anisotropic magnetoresistance (AMR) of Py was utilized to independently confirm the anisotropy crossover observed from the susceptibility measurements. The main advantage of such measurements, compared with the traditional magnetometry, is their high sensitivity to the components of magnetization noncollinear with the magnetic field. For instance, the measurements discussed below were sufficiently sensitive to detect average angles of ∼2–3° between the magnetization and the field. The corresponding deviations from the saturated magnetization value are <0.1%, which is beyond the typical detection limit of the standard magnetometry.

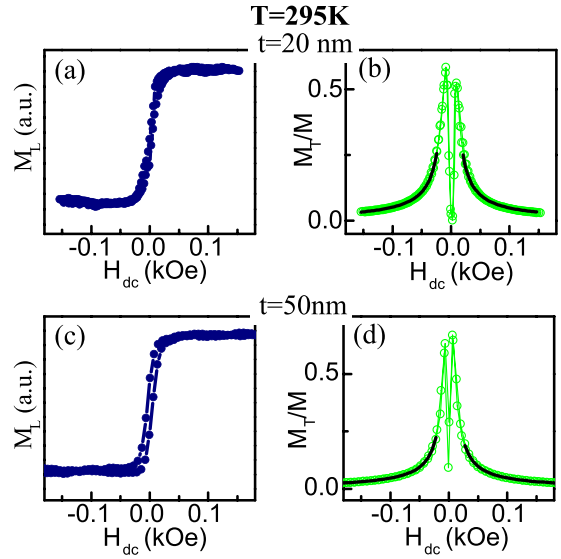

FIG. 2. (a) and (c) Longitudinal dc magneto-optical Kerr effect (MOKE) hysteresis loops and (b) and (d) transverse ac susceptibility acquired at $T = 295$ K for Py(t)/CoO(8) bilayers with (a) and (b) $t = 20$ nm and (c) and (d) $t = 50$ nm.

The measurements were performed in the four-probe van der Pauw geometry, with the current flowing in the direction of the long side of the 6 × 2 mm rectangular sample. ac current with rms amplitude 0.1 mA at the frequency of 1.3 kHz was applied to the sample, and the ac voltage was detected by the lock-in amplifier.

AMR is 180° periodic with respect to the angle between the magnetization **M** and the direction of electrical current I flowing through Py and is minimized when they are orthogonal. In our measurements, the in-plane field was precisely aligned orthogonal to the direction of current by utilizing the dependence of AMR on the field direction at RT. Alignment precision of ∼1° was limited by the resolution of the electronic measurement. In this geometry, the dependence of resistance on the angle θ between the field and the magnetization M of Py is described by $R(\theta) = R_0 + \Delta R \sin^2(\theta)$, where R_0 is the resistance minimum at $\theta = 0°$, and ΔR is the magnetoresistance. This measurement is sensitive to the component of **M** noncollinear with $\mathbf{H}_{dc}$, with the resistance increase proportional to average θ^2.

III. EXPERIMENTAL RESULTS

A. Magnetic hysteresis and ac susceptibility

We start with the measurements at RT $T = 295$ K above the Néel temperature $T_N = 290$ K of CoO. In this case, the magnetic properties of Py/CoO are expected to be similar to those of standalone Py films. Indeed, the longitudinal dc MOKE hysteresis curves are consistent with the soft low-anisotropy magnetic properties of Py [Figs. 2(a) and 2(c)]. The

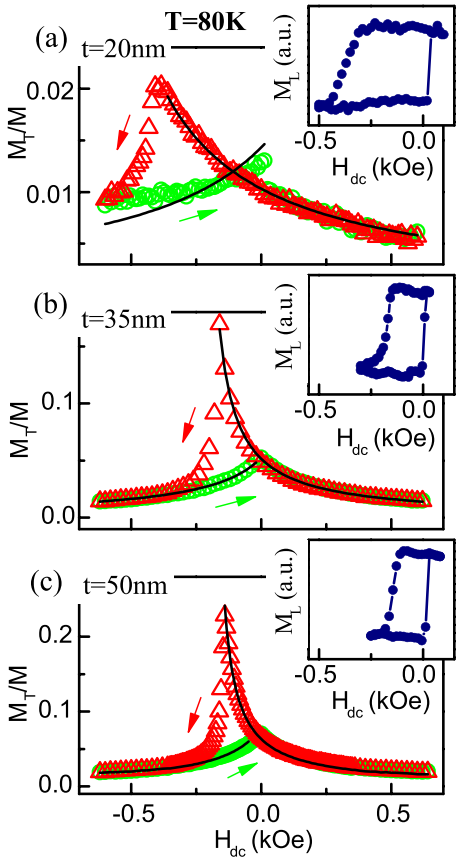

FIG. 3. Ac susceptibility vs dc field for Py(t)/CoO(8) bilayers with Py thicknesses (a) $t = 20$ nm, (b) $t = 35$ nm, and (c) $t = 50$ nm, measured at $T = 80$ K. Symbols are data, curves are fits as described in the text. Insets show longitudinal magneto-optical Kerr effect (MOKE) hysteresis loops acquired simultaneously with the ac susceptibility. Arrows show the directions of the field sweeps.

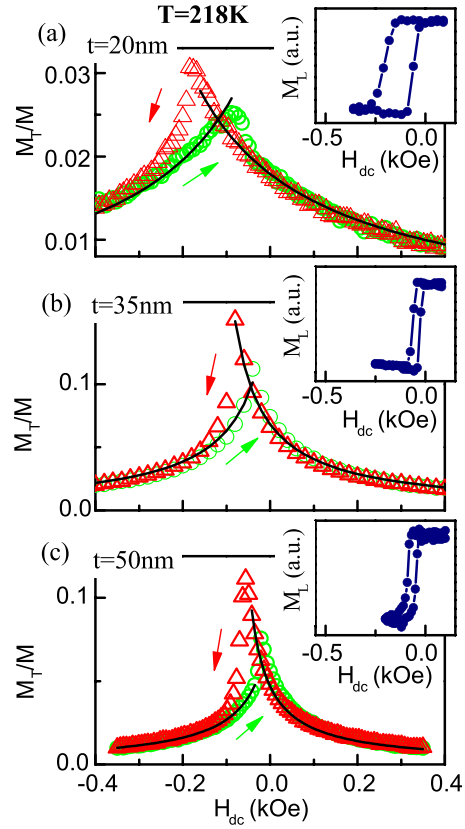

FIG. 4. Same as Fig. 3, at $T = 218$ K.

transverse ac susceptibility curves [Figs. 2(b) and 2(d)] exhibited negligible hysteresis, sharply peaking at $H_{\rm dc}$ approaching 0, as expected from Eq. (1) for negligible anisotropy, i.e., $H_{\rm eff} = H_{\rm dc}$. Large dips at $H_{\rm dc} = 0$ are associated with the formation of a multidomain state during the magnetization reversal, resulting in vanishing susceptibility at ac fields below the DW depinning.

Fitting of the ac susceptibility data with Eq. (1) [curves in Figs. 2(b) and 2(d)] yielded negligible effective anisotropy fields. We used the scaling between M_T/M and the measured ac magneto-optic signals inferred from the fitting for the analysis of low-temperature data. This reduced the number of fitting parameters to one (the anisotropy field), minimizing the fitting uncertainty. Separate tests for standalone Py films showed that the temperature dependence of the magneto-optic coefficients was negligible.

Figure 3 shows the results for $T = 80$ K, for Py thicknesses $t = 20$, 35, and 50 nm. The longitudinal MOKE hysteresis loops shown in the insets illustrate that the samples exhibit well-defined switching between two reversed orientations of **M**. The coercive fields H_{C1} and H_{C2} determined from the dc MOKE hysteresis loops coincide with the peaks in the corresponding branches of the ac susceptibility curves, consistent with the calculations in Fig. 1(c). All three samples exhibit directional asymmetry of dc MOKE hysteresis loops characterized by the effective EB fields $H_E = -(H_{C1} + H_{C2})/2$ of 185, 80, and 62 Oe for $t = 20$, 35, and 50 nm, respectively. The EB field scales approximately inversely with t, consistent with the averaging of the effects of the FM/AFM interface over the Py film thickness.

The magneto-optic imaging discussed below shows that magnetization reversal occurs via propagation of DWs separating two oppositely magnetized states, resulting in perfectly square hysteresis loops obtained by averaging the magneto-optical images of 65×65 μm sample regions (see Fig. 5). Small deviations from the square shape of the hysteresis loops in Fig. 3 are thus associated with the local variations of DW nucleation and propagation thresholds in different sample regions, resulting in multidomain intermediate states of Py. Analysis of the field dependence of susceptibility described below was performed using the decreasing-field-magnitude branches of the hysteresis curves, corresponding to the quasi-uniform magnetization states.

The susceptibility data for $t = 20$ nm [Fig. 3(a)] are consistent with the presence of unidirectional anisotropy. Indeed, the asymmetry of susceptibility can be approximately described as a shift in the negative-field direction, as expected due to the positive effective EB field $H_{\rm ud}$. The data for $t = 35$ and 50 nm [Figs. 3(b) and 3(c)] also exhibit a noticeable asymmetry. However, this asymmetry is predominantly associated with the hysteretic magnetization reversal. As discussed above, the hysteresis is likely associated with inhomogeneous states

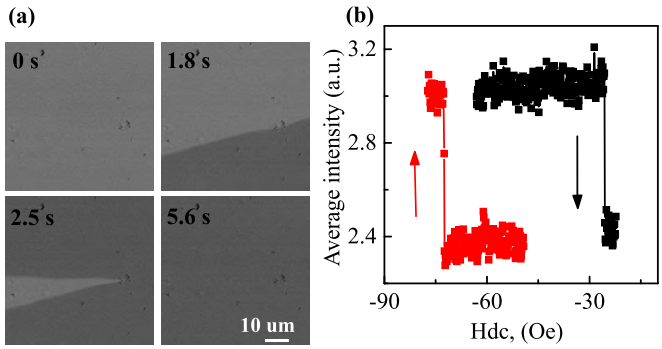

FIG. 5. (a) Representative magneto-optical Kerr effect (MOKE) snapshots of a 65 × 65 μm area for the Py(35)CoO(8) sample, capturing its magnetization reversal at the labeled instants of time. The images were acquired at $T = 218$ K, with the horizontal dc field slowly swept at a rate of 0.14 Oe/s from the initial value of −23.7 Oe. (b) Partial MOKE hysteresis loops obtained by averaging the intensities over the images such as those in (a).

involved in the reversal process, whose response to ac field is dependent on the spatial magnetization distribution. To avoid this complication, we focus only on the dependence of susceptibility on H_{dc} for the quasi-uniform magnetization states, obtained when the field magnitude is decreased from large saturating values. For these branches, the susceptibility is almost symmetric with respect to the field direction. We conclude that *the effective unidirectional anisotropy field essentially vanishes, despite a significant asymmetry of the hysteresis loops*.

We note that, for $t = 20$ nm [Fig. 3(a)], the peak of transverse susceptibility in the upward field sweep is significantly smaller than in the downward sweep. For $t = 35$ and 50 nm [Figs. 3(b) and 3(c)], the asymmetry is even more dramatic, as the peak in the upward sweep is replaced by the nonhysteretic crossover to the downward-sweep branch. We will discuss our interpretation of these behaviors in the next section.

We quantified the effective exchange fields by fitting the decreasing-field-magnitude branches of susceptibility curves with Eq. (1). This equation provided excellent fitting for all the data, except for the negative-field branch for $t = 20$ nm [Fig. 3(a)]. In the latter case, the fitting curve underestimated the susceptibility at large negative fields and overestimated it at small fields. This discrepancy is explained by a significant inhomogeneity of the magnetization state due to the torques exerted on **M** by the AFM, as discussed in the next section. The values of the effective unidirectional anisotropy field H_{ud} obtained from the fitting are 110, 0, and 20 Oe for $t = 20$, 35, and 50 nm, respectively. The vanishing unidirectional anisotropy for thick Py is consistent with the qualitative analysis above.

For the uniaxial anisotropy, we obtain $H_{ua} = 670$, 230, and 170 Oe for $t = 20$, 35, and 50 nm, respectively. In contrast to the H_{ud}, H_{ua} does not abruptly vanish with increasing Py thickness. Its gradual decrease with increasing t is consistent with the diminishing effects of the AFM on the thicker Py films.

We have performed similar measurements at other temperatures to ascertain that the observed crossover of magnetic anisotropy is a robust characteristic of the studied structures. Figure 4 shows the results for $T = 218$ K, which is the base temperature of the magneto-optical imaging discussed below. This temperature is much closer to the Néel temperature $T_N = 290$ K of CoO, and consequently, the EB effects are significantly smaller than at 80 K. Nevertheless, a shift of the longitudinal hysteresis loops in the negative-field direction is apparent. Fitting the susceptibility curves with Eq. (1) yields $H_{ud} = 120$ Oe for $t = 20$ nm, and 20 Oe for $t = 50$ nm. We note that the unidirectional anisotropy is almost unchanged from $T = 80$ K, even though the EB is significantly smaller. In the rest of this paper, we present complementary measurements, analysis, and simulations that elucidate the microscopic mechanisms of these behaviors.

B. Magneto-optic imaging of magnetization reversal

To ascertain that the surprising effects observed in the ac susceptibility measurements are not associated with some complex disordered magnetization states, we performed real-time magneto-optical imaging of the magnetization reversal process with a slowly swept field. Figure 5 shows the images representative of all the studied samples, for both directions of magnetization reversal. We have repeated measurements over different sample regions to verify that our observations are representative. For both field sweep directions, the reversal typically proceeded via the sweep of a nearly straight DW. In the less-typical instance shown in Fig. 5(a), an upward-propagating DW was stopped by a defect in the middle-right part of the image, and the reversal proceeded via a downward-propagating DW. Nevertheless, the entire reversal was completed within the 1 Oe range of H_{dc}.

No significant DW roughness or distortions during propagation were observed, consistent with weak magnetization pinning by defects. The magnetization in the regions separated by the DW is uniformly saturated in the opposite directions, as is also evident from the square partial hysteresis loop obtained by averaging the MOKE intensity over the image area [Fig. 4(c)]. Based on these results, we conclude that the studied systems remain quasi-uniformly magnetized except for reversal, validating the presented analysis of anisotropy based on the transverse susceptibility measurements.

C. Characterization of magnetization state by AMR

Magnetoelectronic measurements utilizing AMR independently confirmed the surprising dependence of anisotropy on the Py thickness observed in the transverse susceptibility measurements. Figure 6 shows representative AMR hysteresis loops for $t = 20$ and 50 nm acquired at $T = 80$ K, the base temperature of our transverse susceptibility measurements.

In our measurements, the current direction was orthogonal to the cooling field H_{cool}. Thus, in measurements with $\mathbf{H}_{dc} \parallel \mathbf{H}_{cool}$ shown in panels (a) and (c), the resistance R was minimized when the magnetization was saturated in the direction of the field. Deviations from saturation are detected as a resistance increase, which is approximately proportional to $\langle\theta^2\rangle$, the average of the square of the angle between **M** and $\mathbf{H}_{dc}$. Conversely, for $\mathbf{H}_{dc} \perp \mathbf{H}_{cool}$ [panels (b) and (d)], R

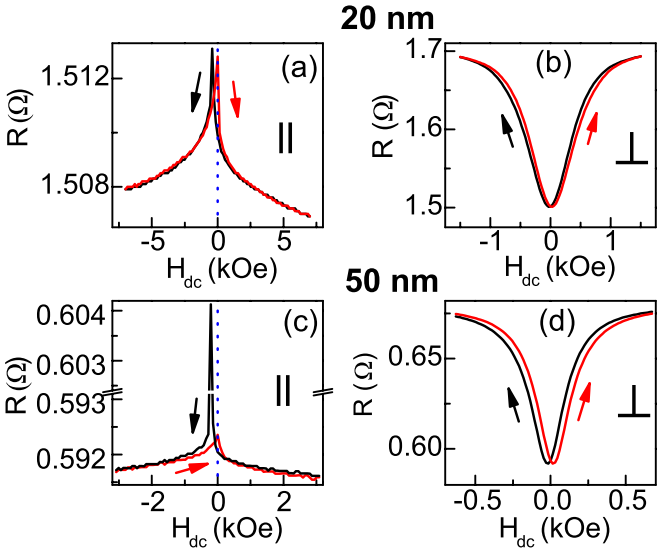

FIG. 6. Anisotropic magnetoresistance (AMR) vs H_{dc} for the Py thickness (a) and (b) $t = 20$ nm and (c) and (d) $t = 50$ nm acquired with the field direction (a) and (c) parallel and (b) and (d) perpendicular to the cooling field, at $T = 80$ K. The current flows perpendicular to the cooling field. The dotted vertical lines in (a) and (c) show $H_{dc} = 0$.

decreases when the magnetization deviates from the direction of the field.

To facilitate direct comparison between the data for different Py thicknesses, the horizontal (field) scales in panels (a) and (b) are 2.5 times larger than in panels (c) and (d). This accounted for the 2.5 times smaller Py thickness in these panels, resulting in smaller effects of H_{dc} relative to those of the effective exchange fields at the FM/AFM interface. Similarly, we adjusted the vertical (resistance) scales to account for the different values of magnetoresistance of the two samples. Specifically, the AMR of the sample with $t = 20$ nm is 0.2 Ω, while the AMR of the sample with $t = 50$ nm is 0.085 Ω. Accordingly, the vertical scales in panels (a) and (b) are 2.3 times larger than in panels (c) and (d), respectively.

The appropriateness of such scaling is evident from the data for $\mathbf{H}_{dc} \perp \mathbf{H}_{cool}$, which are nearly identical for two different thicknesses. In this case, as the magnitude of $\mathbf{H}_{dc} \perp \mathbf{H}_{cool}$ is decreased, R gradually and almost nonhysteretically decreases, at $H_{dc} = 0$ almost reaching its minimal value achieved at large $\mathbf{H}_{dc} \parallel \mathbf{H}_{cool}$ [compare with panels (a) and (c)]. Thus, at small H_{dc}, the magnetization forms a quasiuniform configuration orthogonal to H_{dc}, consistent with the dominant effects of H_{ua} and/or H_{ud}.

The results for $\mathbf{H}_{dc} \parallel \mathbf{H}_{cool}$ are noticeably different for the two thicknesses. For $t = 20$ nm, the heights of the two peaks associated with the reversal are similar, and the asymmetry with respect to the field direction can be approximated as an overall shift, consistent with the unidirectional anisotropy. In contrast, for $t = 50$ nm, at large H_{dc}, the variations of R and the asymmetry between the two directions of H_{dc} are much smaller than for $t = 20$ nm. These results are consistent with our analysis of ac susceptibility. Additionally, the peak associated with the reversal in the downward field sweep is significantly taller than for the upward sweep. The origin of this difference is discussed in the next section.

IV. ANALYSIS AND SIMULATIONS

We first summarize the key observations that do not fit in the common picture of EB as the result of an effective exchange field produced by "frozen" AFM spins at the FM/AFM interface. We then introduce a microscopic picture that captures our observations and present micromagnetic simulations supporting its viability.

A. Qualitative analysis

Our main observation is that, for sufficiently large Py thickness t, the unidirectional anisotropy vanishes, despite a sizable asymmetry of the magnetic hysteresis loop. For instance, for $t = 50$ nm at $T = 80$ K, magnetization reversal occurs at coercive fields $H_{C1} = -146$ Oe and $H_{C2} = 22$ Oe [see inset in Fig. 3(c)], yielding the conventionally defined EB field $H_E = -(H_{C1} + H_{C2})/2 = 62$ Oe and the coercivity $H_C = (H_{C2} - H_{C1})/2 = 84$ Oe. These values are traditionally associated with the unidirectional and uniaxial anisotropies, respectively. However, quantitative characterization of anisotropy by transverse ac susceptibility yields effective unidirectional anisotropy field $H_{ud} = 20$ Oe, >3 times smaller than H_E, while the effective uniaxial field is $H_{ua} = 170$ Oe, twice as large as the coercivity. These effects are confirmed by the analysis of the AMR hysteresis curves, whose asymmetry for large Py thicknesses cannot be described as a shift induced by an effective field.

For $t = 20$ nm, the susceptibility and the AMR data can be approximately described as a shift, but the field dependence of susceptibility significantly deviates from the fitting curve [Fig. 3(a)]. This result cannot be explained by the spatial variations of the magnitude of effective exchange fields with the same orientation. Indeed, for some distribution $H_{eff,i} = \langle H_{eff} \rangle + \Delta H_i$, where ΔH_i is the local deviation of effective field from the average $\langle H_{eff} \rangle$, Taylor expansion of Eq. (1) with respect to $\Delta H_i / \langle H_{eff} \rangle$ yields $\langle M_T/M \rangle \approx H_{ac}/\langle H_{eff} \rangle + \langle \Delta H_i^2 \rangle / \langle H_{eff} \rangle^2$, which describes enhancement of susceptibility at small fields, opposite to the observed trend. These results provide evidence for the deviations of the magnetization state from saturation that become enhanced at small H_{dc}, resulting in reduced susceptibility. However, magneto-optical imaging shows clean switching between two oppositely magnetized saturated magnetization states. Thus, such deviations must be small and/or spatially localized to nanoscale dimensions.

We now introduce a microscopic model that accounts for these seemingly contradictory observations, as well as other puzzling features of our data. We start with the idea of Koon [34] and Schulthess and Butler [35], that the exchange interaction at the FM/AFM interface leads to the AFM spin flop, resulting in uniaxial anisotropy. Indeed, both the susceptibility and the AMR measurements reveal uniaxial anisotropy whose easy axis is well-aligned with the cooling field. The stability of the anisotropy axis implies that the local Néel vector must be frozen by the field-cooling, which is likely facilitated by the random variations of exchange coupling at the FM/AFM

interface that result in a complex AFM energy landscape enabling multiple metastable magnetic configurations, among them the spin-flop configurations favored by the field-cooling.

By itself, this interpretation does not explain EB because the spin-flop state is bistable [35]. To explain the existence of EB in the absence of directional anisotropy, we invoke the argument of Malozemoff [14] that interface imperfections frustrate exchange interaction across the FM/AFM interface. This implies that, upon field-cooling, the direction of the AFM spin flop locally randomly varies around the average defined by the field-cooling.

Consider now the process of the Py magnetization reversal via the DW sweep (see Fig. 5). For the magnetic films with in-plane anisotropy, the DW is of the Néel type, with the magnetization twisted in the DW in plane either clockwise or anticlockwise. During the DW sweep, the direction of the twist becomes imprinted onto the AFM as an asymmetry of spin-flop distribution with respect to the field axis. The effect of this asymmetric distribution on the reversed magnetization **M** of Py is a torque rotating it in the direction opposite to the DW twist. Spatial fluctuations of the FM/AFM exchange coupling must result in local "hotspots" where this torque is large, providing nucleation centers for the reversal of magnetization back into the field-cooled direction, which is expected to occur close to $H_{dc} = 0$, consistent with the data (see Figs. 3 and 4).

The proposed mechanism locally acts as an effective AFM exchange spring that "winds" during initial reversal, and whose unwinding facilitates the reversal of M back into the cooling-field direction, reminiscent of the mechanism proposed by Mauri *et al.* [26]. However, if an actual exchange spring were created in CoO, its wound-state exchange energy E_{ex} per unit area of the film would determine the effective unidirectional field $H_{ud} = E_{ex}/2\mu_0 Mt$. In contrast, the proposed mechanism does not require a difference in the magnetic energy between the two opposite magnetization states, consistent with the lack of unidirectional anisotropy in our measurements for thick Py films. Central to our interpretation of the origin of EB in the studied system is the asymmetry of the magnetization reversal process. Such asymmetry has been extensively reported for a variety of FM/AFM systems, suggesting its general significance for EB [31,45,46].

The proposed mechanism explains the dependence of anisotropy on the Py thickness t as follows. For $t = 20$ nm, the torques exerted by the AFM on **M** result in its more significant twisting than in thicker Py, where the effects of spatially varying the FM/AFM exchange become efficiently averaged through the FM thickness. In turn, this implies that the torques exerted by a thinner FM on the AFM are smaller, resulting in only partial reversal of the spin-flop state in the AFM. Thus, for thin Py, some of the AFM spins remain frozen, in agreement with the conventional picture of EB.

The proposed mechanism also explains why the susceptibility exhibits large peaks only for the decreasing-field branches. For increasing field, the reversal of **M** facilitated by the nucleation at hotspots occurs once the energy of the reversed state becomes lower, i.e., at the crossing of the $H_{dc} < 0$ and $H_{dc} > 0$ branches of susceptibility curves [see Eq. (1)]. For negligible H_{ud}, this is expected to occur at $H_{dc} = 0$, in excellent agreement with the data (Fig. 3).

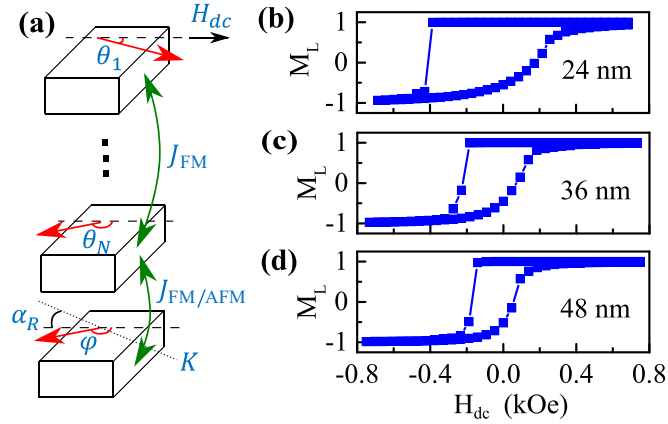

FIG. 7. (a) Schematic of the vertical stack of micromagnetic cells used in the simulations. Straight arrows show the magnetic moments, curved arrows show the interactions. θ_i, $i = 1..N$ is the angle between $\mathbf{H}_{dc}$ and the magnetic moment of cell i, ϕ is the angle between $\mathbf{H}_{dc}$ and the magnetic moment of the cell representing the AFM, J_{FM} and $J_{FM/AFM}$ are the exchange interaction constants within the FM and at the FM/AFM interface, respectively, K is the uniaxal anisotropy of the AFM layer, and α_R is the random angle between the easy anisotropy axis and $\mathbf{H}_{dc}$. (b)–(d) Simulated hysteresis loops for the FM thickness $t = 24$, 36, and 48 nm, respectively, as labeled.

B. Micromagnetic simulations

We now present micromagnetic simulations that support the proposed mechanism. The simulations utilized the MUMAX3 software [47–49], using a mesh of micromagnetic cells with dimensions $2.5 \times 2.5 \times 3$ nm, where the third dimension refers to the out-of-plane direction. The simulated area was 320×320 nm, with the Py layer thickness varied between 24 and 48 nm. The magnetic parameters of Py were saturation magnetization $M_{sat} = 8 \times 10^5$ A/m, Gilbert damping constant 0.02, and exchange stiffness $J_{FM} = 13 \times 10^{-12}$ J/m.

The bistable spin-flop state of the AFM was modeled by a single layer adjacent to the FM, with randomly oriented uniaxial anisotropy of fixed magnitude $K = 550$ kJ/m^3, which provided a good match with the experimental hysteresis loops. The exchange constant $J_{FM/AFM}$ for the interaction between this layer and the FM was the same as within the FM, but the exchange between the cells representing the AFM was neglected. A similar approximation is utilized in the "granular" models of EB [50–52]. The parameters and the interactions through the vertical stack of the micromagnetic cells are schematically shown in Fig. 7(a).

At the start of the simulations, the magnetic moments of all the cells, including the FM and AFM, were initialized in a uniform state with $\varphi = \theta_i = 0$ (see Fig. 7 for the nomenclature) that defined the field-cooling direction, and the system was then allowed to relax. The field H_{dc} was applied at a small positive angle relative to this direction to simulate the directional asymmetry induced by the reversal via the DW sweep. To determine the stationary state for a given H_{dc}, the system was allowed to relax until its dynamics became negligible.

Panels (b)–(d) in Fig. 7 show the simulated hysteresis loops for the Py thicknesses $t = 24$, 36, and 48 nm, respectively, close to the values utilized in our measurements. All three loops exhibit directional asymmetry and enhanced coercivity which decrease with increasing t, consistent with the experimental observations. Furthermore, the coercive fields are in agreement with those measured for similar values of t. However, the gradual reversal into the field-cooling direction and the abrupt reversal against it are opposite to the experimental trends. These differences are likely associated with the neglected effects of long-range AFM correlations on the magnetic energy landscape, as well as thermal fluctuations.

We now analyze the microscopic mechanisms underlying these switching behaviors, focusing on the distribution of the angle φ between the AFM spins and $\mathbf{H}_{dc}$, for thicknesses $t = 24$ and 48 nm. The initial distribution is centered around $\varphi = 0$ and is the same for both thicknesses [Fig. 8(a)], as determined by the initial simulation conditions and the distribution of uniaxial anisotropy.

In the reversed state, the distribution for $t = 48$ nm is dominated by a peak around $\varphi = 180°$, i.e., nearly all of the AFM spins become reversed, and the directional anisotropy associated with the frozen AFM spins is negligible [open symbols in Fig. 8(b)]. In addition, there is a bump at small φ but no such feature near $\varphi = 360°$. This directional asymmetry is associated with the rotation sense of $\mathbf{M}$ during reversal, defined by a small tilt of $\mathbf{H}_{dc}$ relative to $\mathbf{H}_{cool}$. A spatial map of $|\sin\varphi|$, which determines the torque exerted by the AFM spins on the saturated $\mathbf{M}$, exhibits hotspots that serve as nucleation centers for reversal into the field-cooled state.

The unidirectional anisotropy of the FM due to the unflipped AFM spins is given by $[\cos\varphi^{(i)} + \cos\varphi^{(f)}]/2$, where $\varphi^{(i)}$ ($\varphi^{(f)}$) is the AFM spin angle in the initial (reversed) state. The corresponding map also exhibits hotspots, Fig. 8(d). However, the characteristic magnitudes are small, consistent with the experiment.

In contrast to $t = 48$ nm, for $t = 24$ nm, the AFM spin distribution forms a broad peak between $\varphi = 0$ and $\sim 200°$, substantially breaking the rotational symmetry [open symbols in Fig. 8(b)]. Just like for $t = 48$ nm, the spatial distribution of torques forms hotspots that serve as reversal nucleation centers [Fig. 8(e)]. However, in this case, φ is broadly distributed over a large range of angles instead of being concentrated around 0 and 180°. As a consequence, both the torques and the unidirectional anisotropy are substantially larger [Figs. 8(e) and 8(f)].

The large spatially inhomogeneous torques exerted by this AFM spin distribution on $\mathbf{M}$ result in significant deviations of the latter from the direction of H_{dc}, consistent with our experimental data. They also explain a surprising recent observation that the effective exchange field in CoO/Py bilayers with a thin Py is spatially uncorrelated only for $\mathbf{M} \parallel \mathbf{H}_{cool}$ but is correlated on the scale of the magnetic exchange length for the opposite direction of $\mathbf{M}$ [15]. Indeed, the distribution in Fig. 8(b) for $t = 24$ nm is substantially asymmetric, resulting in spatially correlated torques on the Py magnetization.

Our analysis also explains the thickness-dependent asymmetry of the AMR curves. For the 20-nm-thick Py, the EB results mainly in the horizontal shift of the curves since an effective EB field is added to the external field. As a consequence, the peaks are similar in height for both directions. In contrast, for thicker films, EB results in asymmetric reversal without an overall shift of the curves. Reversal into the direction opposite to the cooling field occurs at $H_{dc} < 0$, so that the effects of random exchange fields become large, resulting in a peak of AMR associated with an inhomogeneous magnetization state. In contrast, reversal into the field-cooled direction occurs close to $H_{dc} = 0$, where such effects are smaller.

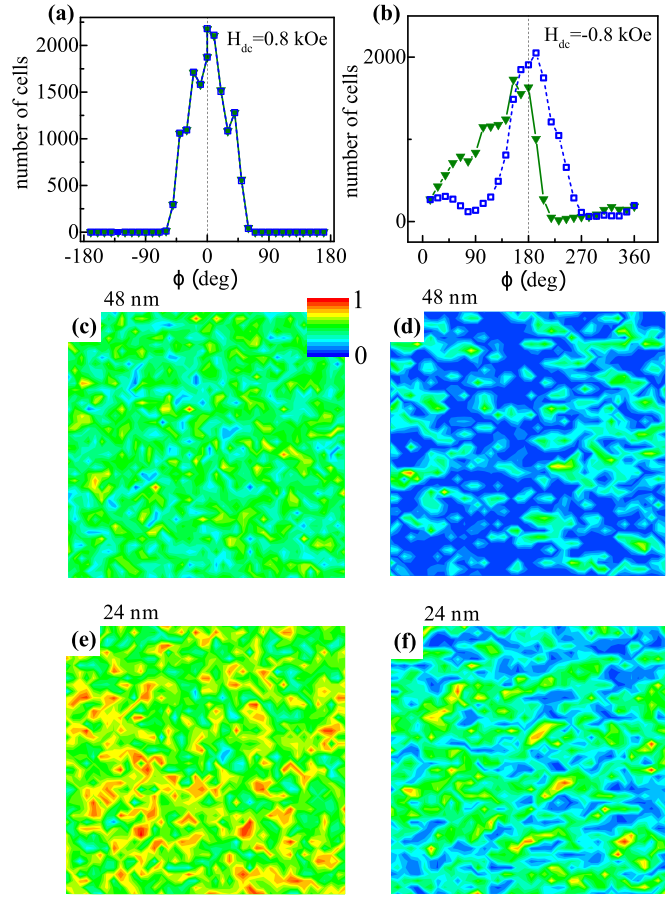

FIG. 8. (a) Simulated distribution of the antiferromagnet (AFM) magnetization angle φ in the initial state at $H_{dc} = 0.8$ kOe, for $t = 24$ nm (symbols) and $t = 48$ nm (curve). (b) Distribution of φ in the reversed state at $H_{dc} = -0.8$ kOe, for $t = 24$ nm (solid symbols) and $t = 48$ nm (open symbols). (c) Representative spatial map of $|\sin\varphi|$, which is proportional to the torque exerted by the AFM on the saturated M in the reversed state for $t = 48$ nm. The map shows the region 320×320 nm utilized in the simulations. (d) Representative spatial map of $[\cos\varphi^{(i)} + \cos\varphi^{(f)}]/2$, which is proportional to AFM-induced unidirectional anisotropy, for $t = 48$ nm, over the same region as in (c). (e) and (f) Same as (c) and (d) for $t = 24$ nm. The scale for the maps (c)–(f) is shown in panel (c).

V. SUMMARY AND OUTLOOK

We have presented several complementary measurements and simulations, which revealed that the magnetization states and reversal mechanisms in a model EB system, a Py/CoO bilayer, are likely dominated by the random distribution of spin flop in CoO. Magnetization reversal becomes imprinted

on this distribution, resulting in hotspots of asymmetric AFM spin distribution that exert local torques on the Py magnetization in exchange springlike fashion. These hotspots serve as DW nucleation centers, facilitating magnetization reversal into the initial field-cooled state. A striking consequence of this mechanism is the negligible unidirectional anisotropy for sufficiently thick Py films, despite a significant directional asymmetry of the magnetic hysteresis loop.

Our findings can be verified by a variety of modern techniques. For instance, the absence of unidirecitonal anisotropy can be verified from the lack of asymmetry of FMR frequency with respect to the direction of external field. Meanwhile, the linewidth is expected to be larger for the field direction opposite to the cooling field due to the inhomogeneous broadening effects. The hotspots of local torques can be detected by nanometer-scale imaging using magnetic force microscopy or magnetic circular dichroism, which should reveal localized twists of magnetization in the direction determined by prior reversal.

Our microscopic picture is substantially different from prior work. Nevertheless, in addition to the AFM spin flop and random field effects, our picture naturally incorporates elements of granular and exchange-spring models of EB, which have been extensively utilized to analyze FM/AFM-based magnetic systems, providing partial validation for these models while also offering microscopic insights into the underlying mechanisms. The effects revealed by our study of CoO/Py are likely present in varied proportions in other EB systems. Our preliminary ac susceptibility measurements of Py/NiO bilayers yield thickness-dependent anisotropy similar to that reported above for Py/CoO.

Both CoO and NiO are characterized by localized magnetic moments and simple two-sublattice magnetic structure with anisotropy defined by the crystal structure. In contrast, technologically important AFM alloys such as IrMn and FeMn are itinerant AFMs, with local anisotropies and magnetic structure likely strongly affected by the alloy disorder. Such disorder may result in the formation of correlated glassy spin states at the interfaces with the FM, partially suppressing the simple spin-flop reversal reported here for CoO. Nevertheless, we expect that the proposed picture of EB as a consequence of the interplay between randomly distributed local anisotropies and spin flop is also relevant for these systems. We also note that, because of the high blocking temperature of IrMn, it is commonly deposited in field on top of the FM to set the direction of EB. This should not influence the microscopic mechanisms reported here for field-cooled systems.

We believe that our results can lead to the development of devices taking advantage of EB beyond the usual magnetization pinning. For instance, this paper has shown that magnetization reversal in the presence of EB does not need to overcome unidirectional or even uniaxial anisotropy barrier. Therefore, efficient reversal can be achieved simply by localizing the mechanism driving the reversal, such as the electric field [53] or strain [54], to a small hotspot region of the device.

Our findings are encouraging for the development of FM/AFM-based magnetic memristors [7,13]. It was recently suggested that an ideal memristor can be implemented based on FM/AFM bilayers by utilizing viscous dynamics of Néel order close to the AB blocking temperature T_B [12]. Similarly, a proof-of-principle implementation of FM/AFM bilayer-based magnetic memristor required operation close to T_B [13], severely limiting thermal compliance of such devices. Our results indicate that these requirements can be eliminated by taking advantage of the bistable spin-flop state of the AFM as an atomic-scale multilevel memory mechanism. As is evident from Fig. 8, the distribution of AFM spin-flop states reflects the history of the FM magnetization dynamics, making this system well-suited for memristive applications.

The dynamics of AFM spin-flop reversal in FM/AFM heterostructures is likely governed by the high dynamical frequencies of the AFM. The energy scale involved in this dynamics is of the order of exchange energy, i.e., $\sim$100 mV per pair of interfacial spins. Thus, fast multistable devices are achievable in the deep nanoscale regime. Efficient implementations of such devices will likely rely on the ability to tailor the magnetic properties and the interaction strengths to enable efficient and fast driving of the AFM spin-flop reversal during memristor writing, while retaining long-term stability in the absence of driving.

ACKNOWLEDGMENTS

We acknowledge support by the National Science Foundation Award No. ECCS-2005786.

[1] S. N. Piramanayagam, *Developments in Data Storage: Materials Perspective* (Wiley IEEE Press, Hoboken, Salem, 2012).
[2] R. H. Victora and Xiao Shen, IEEE Trans. Magn. **41**, 537 (2005).
[3] B. Tudu and A. Tiwari, Vacuum **146**, 329 (2017).
[4] A. A. Timopheev, B. M. S. Teixeira, R. C. Sousa, S. Aufret, T. N. Nguyen, L. D. Buda-Prejbeanu, M. Chshiev, N. A. Sobolev, and B. Dieny, Phys. Rev. B **96**, 014412 (2017).
[5] K. Nanayakkara, I. S. Vasilevskii, I. S. Eremin, O. S. Kolentsova, N. I. Kargin, A. Anferov, and A. Kozhanov, J. Appl. Phys. **119**, 233906 (2016).
[6] X. Wang, Y. Chen, H. Xi, H. Li, and D. Dimitrov, IEEE Electron Device Lett. **30**, 294 (2009).
[7] Y. V. Pershin and M. Di Ventra, Phys. Rev. B **78**, 113309 (2008).
[8] P. Krzysteczko, G. Reiss, and A. Thomas, Appl. Phys. Lett. **95**, 112508 (2009).
[9] P. Krzysteczko, J. Münchenberger, M. Schäfers, G. Reiss, and A. Thomas, Adv. Mater. **24**, 762 (2012).
[10] L. Balents, Nature (London) **464**, 199 (2010).
[11] K. Binder and A. P. Young, Rev. Mod. Phys. **58**, 801 (1986).
[12] G. Chen, S. Ivanov, and S. Urazhdin, Appl. Phys. Lett. **117**, 103501 (2020).
[13] M. Mansueto, A. Chavent, S. Auffret, I. Joumard, J. Nath, I. M. Miron, U. Ebels, R. C. Sousa, L. D. Buda-Prejbeanu,

I. L. Prejbeanu, and B. Dieny, Phys. Rev. Appl. **12**, 044029 (2019).
[14] A. P. Malozemoff, Phys. Rev. B **35**, 3679 (1987).
[15] G. Chen, D. Collette, and S. Urazhdin, Phys. Rev. B **101**, 144427 (2020).
[16] S. Urazhdin and U. Danilenko, Phys. Rev. B **92**, 174416 (2015).
[17] T. Ma and S. Urazhdin, Phys. Rev. B **97**, 054402 (2018).
[18] T. Ma, X. Cheng, S. Boettcher, S. Urazhdin, and L. Novozhilova, Phys. Rev. B **94**, 024422 (2016).
[19] W. H. Meiklejohn and C. P. Bean, Phys. Rev. **105**, 904 (1957).
[20] J. Nogués and I. K. Schuller, J. Magn. Magn. Mater. **192**, 203 (1999).
[21] M. Kiwi, J. Magn. Magn. Mater. **234**, 584 (2001).
[22] J. Nogués, J. Sort, V. Langlais, V. Skumryev, S. Suriñach, J. Muñoz, and M. Baró, Phys. Rep. **422**, 65 (2005).
[23] R. L. Stamps, J. Phys. D **33**, R247 (2000).
[24] A. Berkowitz and K. Takano, J. Magn. Magn. Mater. **200**, 552 (1999).
[25] S. Giri, M. Patra, and S. Majumdar, J. Phys.: Condens. Matter **23**, 073201 (2011).
[26] D. Mauri, H. C. Siegmann, P. S. Bagus, and E. Kay, J. Appl. Phys. **62**, 3047 (1987).
[27] H. Ohldag, A. Scholl, F. Nolting, E. Arenholz, S. Maat, A. T. Young, M. Carey, and J. Stöhr, Phys. Rev. Lett. **91**, 017203 (2003).
[28] A. Scholl, M. Liberati, E. Arenholz, H. Ohldag, and J. Stöhr, Phys. Rev. Lett. **92**, 247201 (2004).
[29] Y. Imry and S.-k. Ma, Phys. Rev. Lett. **35**, 1399 (1975).
[30] A. E. P. d. Araújo, F. L. A. Machado, A. R. Rodrigues, A. Azevedo, F. M. de Aguiar, J. R. L. de Almeida, S. M. Rezende, and W. F. Egelhoff, J. Appl. Phys. **91**, 7754 (2002).
[31] E. Jiménez, J. Camarero, J. Sort, J. Nogués, N. Mikuszeit, J. M. García-Martín, A. Hoffmann, B. Dieny, and R. Miranda, Phys. Rev. B **80**, 014415 (2009).
[32] A. P. Malozemoff, Phys. Rev. B **37**, 7673 (1988).
[33] S. Urazhdin, W. Li, and L. Novozhilova, J. Magn. Magn. Mater. **476**, 75 (2019).
[34] N. C. Koon, Phys. Rev. Lett. **78**, 4865 (1997).
[35] T. C. Schulthess and W. H. Butler, Phys. Rev. Lett. **81**, 4516 (1998).
[36] Hendrik Ohldag (private communication).
[37] S. Urazhdin, P. Tabor, and W.-L. Lim, Phys. Rev. B **78**, 052403 (2008).
[38] L. Spinu, H. Srikanth, A. Gupta, X. W. Li, and G. Xiao, Phys. Rev. B **62**, 8931 (2000).
[39] L. Spinu, A. Stancu, Y. Kubota, G. Ju, and D. Weller, Phys. Rev. B **68**, 220401(R) (2003).
[40] R. L. Rodriguez-Suarez, L. H. Vilela Leao, F. M. de Aguiar, S. M. Rezende, and A. Azevedo, J. Appl. Phys. **94**, 4544 (2003).
[41] D. Cimpoesu, A. Stancu, and L. Spinu, Phys. Rev. B **76**, 054409 (2007).
[42] Z. Q. Qiu and S. D. Bader, Rev. Sci. Instrum. **71**, 1243 (2000).
[43] I. V. Soldatov and R. Schäfer, Rev. Sci. Instrum. **88**, 073701 (2017).
[44] I. V. Soldatov and R. Schäfer, J. Appl. Phys. **122**, 153906 (2017).
[45] J. McCord, R. Schäfer, R. Mattheis, and K.-U. Barholz, J. Appl. Phys. **93**, 5491 (2003).
[46] V. S. Gornakov, Y. P. Kabanov, O. A. Tikhomirov, V. I. Nikitenko, S. V. Urazhdin, F. Y. Yang, C. L. Chien, A. J. Shapiro, and R. D. Shull, Phys. Rev. B **73**, 184428 (2006).
[47] A. Vansteenkiste, J. Leliaert, M. Dvornik, M. Helsen, F. Garcia-Sanchez, and B. Van Waeyenberge, AIP Adv. **4**, 107133 (2014).
[48] J. Leliaert, B. Van de Wiele, A. Vansteenkiste, L. Laurson, G. Durin, L. Dupré, and B. Van Waeyenberge, J. Appl. Phys. **115**, 233903 (2014).
[49] L. Exl, S. Bance, F. Reichel, T. Schrefl, H. Peter Stimming, and N. J. Mauser, J. Appl. Phys. **115**, 17D118 (2014).
[50] E. Fulcomer and S. H. Charap, J. Appl. Phys. **43**, 4190 (1972).
[51] M. D. Stiles and R. D. McMichael, Phys. Rev. B **59**, 3722 (1999).
[52] K. O'Grady, L. Fernandez-Outon, and G. Vallejo-Fernandez, J. Magn. Magn. Mater. **322**, 883 (2010).
[53] X. He, Y. Wang, N. Wu, A. N. Caruso, E. Vescovo, K. D. Belashchenko, P. A. Dowben, and C. Binek, Nat. Mater. **9**, 579 (2010).
[54] S. Z. Wu, J. Miao, X. G. Xu, W. Yan, R. Reeve, X. H. Zhang, and Y. Jiang, Sci. Rep. **5**, 8905 (2015).